


Large spontaneous valley polarization and high magnetic transition temperature in stable two-dimensional ferrovalley YX_2 ($X=I, Br, \text{ and } Cl$)

Bo Huang,^{*} Wen-Yu Liu,^{*} Xu-Cai Wu, Shu-Zong Li , Hongxing Li, Zhixiong Yang, and Wei-Bing Zhang [†]

Hunan Provincial Key Laboratory of Flexible Electronic Materials Genome Engineering, School of Physics and Electronic Sciences, Changsha University of Science and Technology, Changsha 410114, People's Republic of China

 (Received 16 February 2022; revised 9 October 2022; accepted 9 January 2023; published 24 January 2023)

Ferrovalley materials with spontaneous valley polarization are crucial to valleytronic application. Based on first-principles calculations, we demonstrate that two-dimensional (2D) YX_2 ($X=I, Br, \text{ and } Cl$) in a 2H structure constitutes a series of promising ferrovalley semiconductors with large spontaneous valley polarization and high magnetic transition temperature. Our calculations reveal that YX_2 are dynamically, energetically, thermally and mechanically stable 2D ferromagnetic semiconductors with a magnetic transition temperature about 200 K. Due to the natural noncentrosymmetric structure, intrinsic ferromagnetic order and strong spin orbital coupling, the large spontaneous valley polarizations of 108.98, 57.70, and 22.35 meV are also predicted in single-layer YX_2 ($X=I, Br, \text{ and } Cl$), respectively. The anomalous valley Hall effect is also proposed based on the valley contrasting Berry curvature. Moreover, the ferromagnetism and valley polarization are found to be effectively tuning by applying a biaxial strain. Interestingly, the suppressed valley physics of YBr_2 and YCl_2 can be switched on via applying a moderate compression strain. The present findings promise YX_2 as competitive candidates for the further experimental studies and practical applications in valleytronics.

DOI: [10.1103/PhysRevB.107.045423](https://doi.org/10.1103/PhysRevB.107.045423)

I. INTRODUCTION

Valley, a local energy extreme in the conduction/valence bands, is emerging as a new degree of freedom for next-generation electronic device. Similar to the charge and spin of carriers, valley degree of freedom can be coded, stored, and manipulated information, which is known as valleytronics [1–3]. The current papers about valleytronics mainly focus on two-dimensional (2D) hexagonal materials, such as graphene and 2H-phase transition metal dichalcogenides (TMDs) MX_2 due to their interesting valley-contrasting physics [4–6]. Especially, MX_2 monolayers are the most promising candidates due to the spatial inversion-symmetry-broken and strong spin-orbit-coupling (SOC) effect. The unique structure of MX_2 monolayer leads to two degenerate but inequivalent valley states at K and K_- in the momentum space. Due to the large separation of K/K_- , the valley states can effectively suppress intervalley scatterings of phonon and impurity [1–3,7], which is a benefit to design electronic devices with high storage density and low-energy consumption.

However, pristine TMD monolayers are intrinsically nonmagnetic, two degenerate valleys in the hexagonal Brillouin zone are not polarized due to their time-reversal symmetry. This limits their applications in direct information storage applications [1–3]. Clearly, the essential step in valleytronics is to break the degeneracy between two valleys, that is, to achieve the valley polarization. Nowadays, many external strategies have been proposed to induce valley polarization.

For example, optical pumping is extensively employed in experiments [8,9]. However, since optical pumping is a dynamic process, the induced carrier lifetime is very short, which is unsuitable for valleytronic applications. Although valley polarization induced by an external magnetic field [10–12] is only 0.1–0.2 meV/T. More importantly, these attempts are volatility, which will limit device application seriously. Magnetic proximity and magnetic doping appeared as an alternative approach for nonvolatility application. However, magnetic doping [13] tends to form clusters and increase scattering during carrier transport. The magnetic substrates for magnetic proximity effect [14,15] could enlarge the device size and increase energy consumption.

Recently, 2D ferrovalley materials with spontaneous valley polarization were proposed [16], which provides new opportunities to overcome the shortages mentioned above. The ferrovalley materials with spatial-inversion-symmetry-breaking and long-range ferromagnetism are expected to produce spontaneous valley polarization under the SOC effect. Although some potential ferrovalley materials, such as VSe_2 [16,17], $LaBr_2$ [18], VSi_2N_4 [19], GdI_2 [20], Cr_2Se_3 [21], NdX_2 ($X=Se, S$) [22], and MBr_2 ($M=Ru, Os$) [23] have been reported, the candidates of ferrovalley materials are still scarce at present. Moreover, most of available materials possess small valley polarization and low magnetic transition temperature. In addition, the prominent K/K_- valleys in some ferrovalley materials are not located at the valence-band maximum (VBM) of the energy band. These shortages limit the practical device application of ferrovalley materials. It is, thus, desirable to explore novel 2D ferrovalley materials with large valley polarization and high magnetic transition temperature.

^{*}These authors contributed equally to this work.

[†]Corresponding author: zhangwb@csust.edu.cn

After screening candidate materials in the computational 2D materials database (C2DB) [24,25] using stability and energy gap criterion, we focus on single-layer (SL) 2H-YX₂ ($X = \text{I, Br, and Cl}$). Since there is an unpaired electron in Y atom, an magnetic moment of $1\mu_B$ per atom and strong magnetic exchange interaction between spins are also expected. Moreover, the Y element belongs to the heavy transition metal element and possesses strong spin-orbital coupling effect, a large valley polarization is expected. By using first-principles calculation, we predicted them as a series of potential 2D ferrovalley semiconductors. The phonon dispersion, formation energy, *ab initio* molecular dynamics and elastic constant calculations are also performed to evaluate the stability of SL YX₂. The magnetic exchange interactions and magnetic transition temperatures are also predicted. The valley polarizations of three SL YX₂ ($X = \text{I, Br, and Cl}$) are calculated, and the underlying mechanism is revealed. A spontaneous valley polarization of 109 meV and a Curie temperature about 200 K (Berezinsky-Kosterlitz-Thouless transition temperature of 307 K) are found in case of YI₂. Moreover, Berry curvature is also calculated, and the anomalous valley Hall effect is proposed. Finally, we also explore the effect of biaxial strain on valley splitting and magnetic transition temperature. Our calculations show that single-layer 2H-YX₂ are stable 2D ferrovalley semiconductors with large spontaneous valley polarization and high magnetic transition temperature. These make them promising materials for future valleytronic applications.

II. COMPUTATIONAL DETAILS

The present calculations have been performed using the Vienna *ab initio* simulation package code [26,27] within projector augmented-wave method [28,29]. General gradient approximations in the Perdew-Burke-Ernzerhof (PBE) implementation [30] were employed as the exchange-correlation functional. To better take into account the strong electronic correction of Y-*d* electrons, a simple rotationally invariant density functional theory (DFT) + *U* method [31] with effective Hubbard parameter (*U*-*J*) of 2 eV was used. Meanwhile, we also performed the hybrid functional HSE06 calculations [32,33] for comparison. A plane-wave basis set with a energy cutoff of 500 eV was used in the calculation. A mesh of $9 \times 9 \times 1$ *k* points generated by the scheme of Monkhorst-Pack [34] was used to sample the Brillouin zone. All the atomic coordinates were optimized until the maximum force of all atoms was less than 5×10^{-2} eV/Å. A large vacuum space of, at least, 15 Å was included in the supercell to avoid interaction between images. Band structure calculations are performed using a primitive cell. The phonon calculations

have been performed using the finite displacement approach, as implemented in the PHONOPY code [35] in which a $2 \times 2 \times 1$ supercell were employed. Furthermore, we have performed *ab initio* molecular dynamics simulations at 300 K in a canonical ensemble using a Nosé heat bath scheme to examine the thermal stability of SL YX₂. In these calculations, a large supercell of (4×4) was used to minimize the constraint of periodic boundary condition. To calculate the Berry curvature and anomalous Hall conductivity, the maximally localized Wannier functions implemented in the WANNIER90 package [36,37] was employed.

The high-order-nearest-neighbor magnetic exchange coupling constants are evaluated by magnetic force theory (MFT) [38–40]. The calculation is performed using the OPENMX [41] software package, which is based on density functional theory and linear combination of pseudoatomic orbitals. The full-band Hamiltonian obtained from OPENMX is used for MFT calculations as implemented in the code Jx [42,43], which provides a way to calculate exchange coupling parameters J_{ij} between two localized spins based on Green's function representation of the Liechtenstein formula. The cutoff radii of Y, I, Br, and Cl are chosen as 10.0, 7.0, 7.0, and 7.0 a.u., respectively. A $10 \times 10 \times 1$ *k* mesh is used for the MFT calculation.

III. RESULTS AND DISCUSSION

A. Structure and stability

As shown in Figs. 1(a) and 1(b), SL 2H-YX₂ ($X = \text{I, Br, and Cl}$) possess a hexagonal cell with space-group $P\bar{6}m2$ (No. 187) in which the inversion symmetry is absent. It contains one Y atom layer and two X atom layers where each Y atom is surrounded by six X atoms to form a trigonal prism. As given in Table I, the lattice constants of SL YX₂ are 4.086, 3.949, and 3.853 Å, respectively. The lattice constants of SL YX₂ increase with the element number of X, which can be attributed to the increasing atomic radius and the weakening reactivity of X atoms.

To evaluate the stability of SL YX₂, we have performed the phonon dispersion, formation energy, molecular dynamics, and elastic constant calculations. As shown in Figs. 1(d) to 1(f), the imaginary frequency is found to be absent in the whole Brillouin zone, indicating that three SL YX₂ are dynamically stable.

We also calculated the formation energy (E_f) of YX₂ defined as $E_f = (E_Y + 2E_X - E_{YX_2})/3$ in which E_{YX_2} represents the total energy of SL YX₂, whereas E_Y and E_X are the energies per Y and X atoms in their most stable bulk structures. According to the definition, a positive formation energy means that the structure is energetically stable. The

TABLE I. The calculated lattice constants, elastic constant, valley polarization (Δ_{val}), magnetic exchange interaction (*J*), and Curie temperature for YX₂ ($X = \text{I, Br, and Cl}$).

Material	a_0 (Å)	$C_{11/22}$ (kbar)	C_{12} (kbar)	C_{44} (kbar)	Δ_{val} (meV)	<i>J</i>	T_c (K)
YI ₂	4.086	76.41	38.94	23.74	108.98	19.80	230
YBr ₂	3.949	118.72	43.87	37.43	57.70	18.68	220
YCl ₂	3.853	127.25	54.40	36.43	22.35	18.07	210

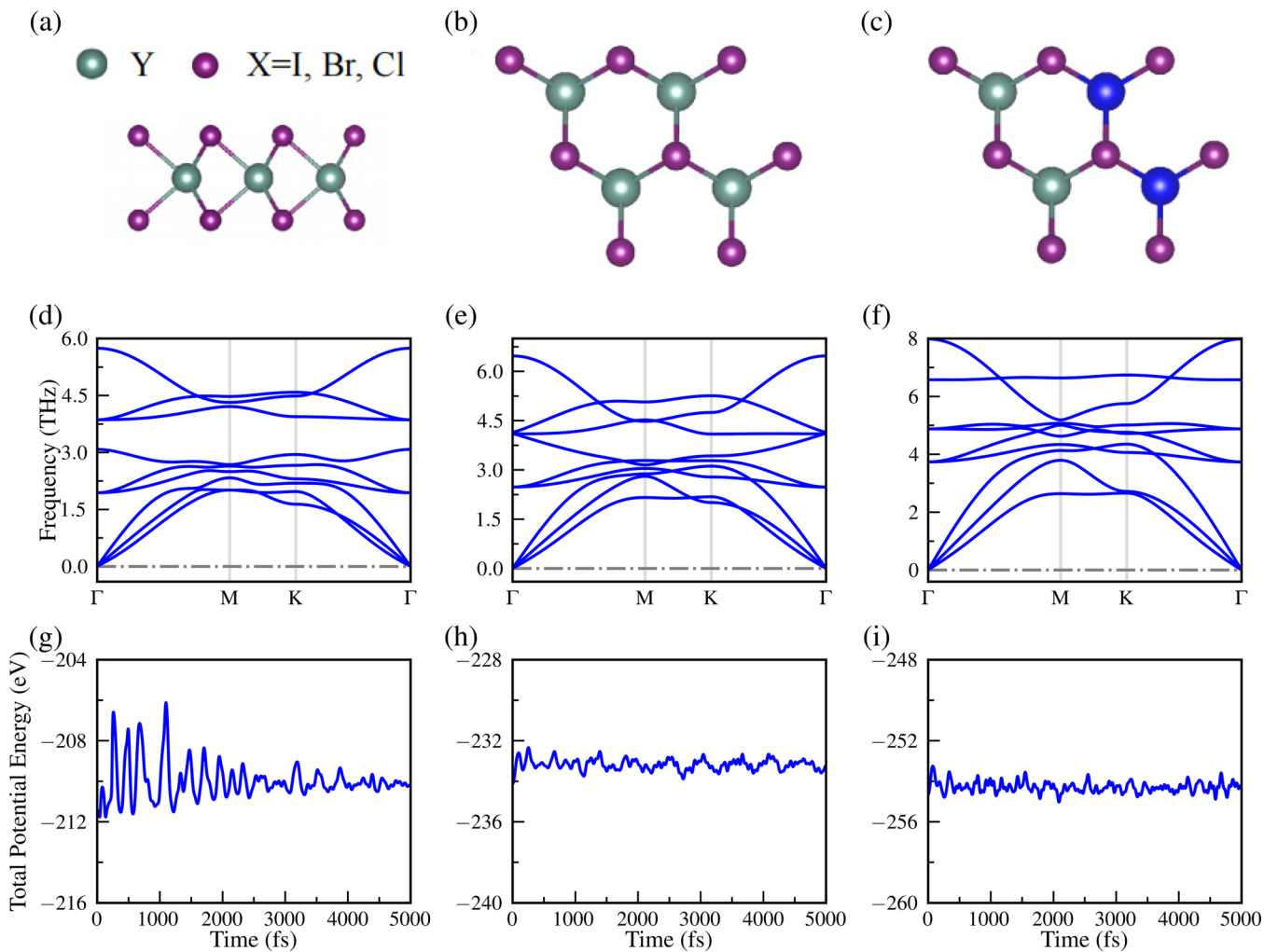


FIG. 1. Geometry and stability of SL YX_2 . The (a) side and (b) top view of structure of SL YX_2 . (c) The antiferromagnetic magnetic configuration in a 2×2 supercell in which the atoms with different spin directions are labeled by different colors. Phonon spectrum of YI_2 , YBr_2 , and YCl_2 are given in (d)–(f), respectively. Variations of the total potential energy of SL YX_2 in the (4×4) supercell with respect to simulation time during *ab initio* molecular dynamics simulations are shown in (g)–(i).

calculated E_f of YI_2 , YBr_2 , and YCl_2 are -1.29 , -1.72 , and -2.02 eV/atom, implying energetical stability of YX_2 . Moreover, room-temperature *ab initio* molecular dynamics results also indicate total potential energies of SL YX_2 remain almost invariant during the simulation [Figs. 1(g)–1(i)], which suggests that these SL YX_2 are thermally stable at 300 K. In addition, according to the Born criteria [44], the elastic constants of stable 2D materials should fulfill the conditions $C_{11}C_{22} - C_{12}^2 > 0$ and $C_{44} > 0$. As shown in Table I, these conditions are satisfied for all three YX_2 's. Clearly, the dynamical, energetical, thermal, and mechanical stability suggest that YX_2 can be realized experimentally even at room temperature.

B. Magnetic property

According to the crystal-field theory, the d orbital in the trigonal environment will be split into $A_1(d_{z^2})$, $E_1(d_{xy}, d_{x^2-y^2})$, $E_2(d_{xz}, d_{yz})$. The electron configuration of a Y^{2+} in YX_2 should be $4d^1$. Clearly, the only one unpaired electron will occupy the lowest-energy d_{z^2} orbital whereas the other orbitals

are empty [Fig. 2(a)]. This unique electron configuration will lead to a spin-polarized ground state, and the magnetic moment of each Y atom is expected to be $1\mu_B$.

To confirm the magnetic ground state of SL YX_2 , we considered ferromagnetic (FM) and antiferromagnetic (AFM) state constructed in a $2 \times 2 \times 1$ supercell as shown in Figs. 1(b) and 1(c). The FM state is found to be the magnetic ground state of YX_2 , followed by the AFM state [Fig. 2(b)]. The energies of FM state are 18.07(208.74), 18.68(174.51), and 19.80(124.51) meV lower than those of the AFM [non-magnetic (NM) state] for YCl_2 , YBr_2 , and YI_2 , respectively. We have calculated the energy difference between FM and AFM with different U - J parameters. The energy-lowest ferromagnetic configuration is found to be independent on the U - J parameters. Our calculations also predict a total magnetic moment of $1\mu_B$ per YX_2 unit cell, which is in good agreement with the above analysis. The following discussions focus on the FM ground state mainly.

To reveal the underlying magnetic mechanism of YX_2 , the nearest neighbor (NN) exchange interactions are extracted by fitting the total energies from DFT calculations for FM and

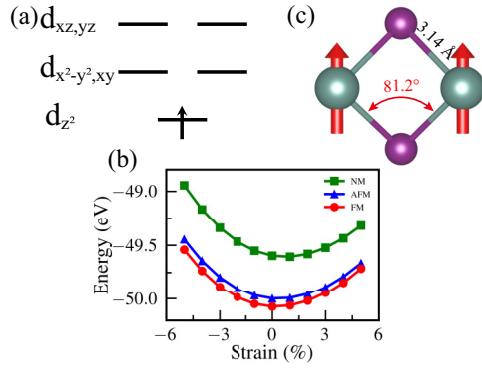


FIG. 2. Electronic configuration and magnetic exchange interaction of single-layer YI_2 . (a) The splitting of d orbitals under the trigonal environment. (b) The change in total energy in different magnetic phases of YI_2 as a function of biaxial strain. (c) The paths for the mediation of nearest-neighbor magnetic exchange interactions in SL YI_2 .

AFM states to the following spin Hamiltonian:

$$H = -J \sum_{\langle ij \rangle} \vec{S}_i \cdot \vec{S}_j, \quad (1)$$

where J is the exchange coupling constant and spin magnetic quantum number $\vec{S} = 1/2$. Considered the fact that the distance between two NN Y atoms in single-layer YI_2 is 4.086 Å whereas next-nearest-neighbor (NNN) distance is 7.077 Å. NNN interaction is expected to be too weak to be considered. Following the routine strategy in other 2H-ferromagnetic monolayers [17,18,20], we also have only considered the nearest neighbors here. The effect of high-order neighbor to magnetic properties will be discussed hereinafter.

The magnetic energy of four YX_2 formulas can be explicitly expressed as

$$E_{FM} = E_0 - 12J\vec{S}^2, \quad (2)$$

$$E_{AFM} = E_0 + 4J\vec{S}^2. \quad (3)$$

As listed in Table I, the NN exchange interaction J is predicted to be ferromagnetic. As shown in Fig. 2(c), the Y-X-Y ($X = I, Br, \text{ and } Cl$) bonding angles are 81° , 84° , and 86° . Based on the Goodenough-Kanamori-Anderson rules [45], ferromagnetic superexchange interaction with near 90° would dominate the interaction between Y atoms, thereby leading to the FM coupling.

Magnetocrystalline anisotropy (MA) is one of the most fundamental properties of magnetic materials. Due to the spin-orbital coupling effect, the total energies of system depend on the direction of magnetic moment. For single-layer YX_2 with trigonal symmetry, the MAE can be analyzed in the following model: $E = K_1 \sin^2 \theta + K_2 \sin^4 \theta$ in which polar angle θ represents the angle with respect to the z axis.

We have calculated the total energies of single-layer YX_2 with the magnetic moment in different directions with an interval of 30° . The direction-dependent energy landscapes are shown in Fig. 3. We find that YI_2 and YBr_2 have easy magnetization planes whereas YCl_2 has an easy axis along the c axis. The energy differences between the z and the x axes

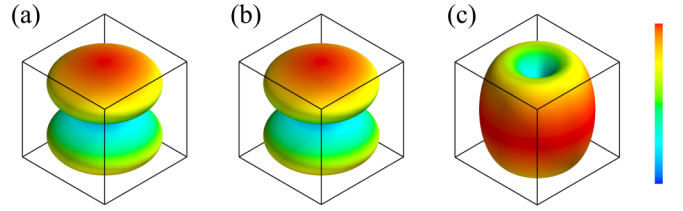


FIG. 3. The anisotropy-energy landscapes of single-layer YX_2 . (a)–(c) represent the YI_2 , YBr_2 , and YCl_2 , respectively.

are 0.44, 0.093, and -0.001 meV for YI_2 , YBr_2 , and YCl_2 , respectively. This indicates that YI_2 and YBr_2 belong to the family of 2D XY magnets whereas YCl_2 belongs to the 2D ISING ferromagnet.

For 2D XY magnets, Berezinsky-Kosterlitz-Thouless (BKT) transition is expected to occur at a critical temperature (T_{BKT}), which can be estimated as $1.335 J/k_B$, where the k_B is the Boltzmann constant. On a basis of the magnetic exchange interaction J , the magnetic transition temperature of YI_2 and YBr_2 is estimated to be 307, 289, and 280 K, respectively.

Considered the tiny MAE and uncertainty of DFT calculation, we also evaluate the critical temperature for ferromagnetism-paramagnetism phase transition. Using these DFT-derived magnetic exchange parameters and the ISING spin Hamiltonian in Eq. (1), the Curie temperature is then estimated using a $80 \times 80 \times 1$ supercell with periodic boundary conditions. For each temperature studied, the MC simulation involves for 10^5 MC steps per site to attain thermal equilibrium. The temperature-dependent mean magnetic moment and magnetic susceptibility are then obtained. The temperature at which the mean magnetic moment drops drastically to nearly zero and the magnetic susceptibility peaks sharply is identified as the Curie temperature. As shown in Fig. 4, the Curie temperature (T_c) of SL YI_2 , YBr_2 , and YCl_2 are about 220, 210, and 200 K, respectively.

In order to evaluate the role of high-order neighbor magnetic exchange interaction to magnetic properties, we calculate the exchange coupling constants from the NN to the 14th NN based on MFT. As shown in Figs. 5(a)–5(c), we can see that the NN magnetic exchange interaction is ferromagnetic whereas the NNNs are antiferromagnetic. The magnetic exchange interaction converges to zero with a neighbor. The NN magnetic exchange coupling constant J_1 of YI_2 , YBr_2 , and YCl_2 are 4.86, 2.69, and 2.11 meV, whereas the corresponding NNN exchange coupling constant J_2 are -0.29 , -0.13 , and -0.09 meV, which is about 20 times smaller than NN interaction.

Moreover, we also estimate the Curie temperature by using the mean-field approximation on a basis of the calculated magnetic exchange coupling constants. The Curie temperature (T_C can be obtained from the maximum eigenvalue of the following eigenvalue equation [46]:

$$T \langle \vec{s}_i \rangle_z = \frac{2}{3k_B} \sum_{jR \neq iO} J_{iO,jR} \langle \vec{s}_j \rangle_z, \quad (4)$$

where k_B is the Boltzmann constant, $J_{iO,jR}$ represents the exchange coupling constant between site i in unit O and site j in unit R .

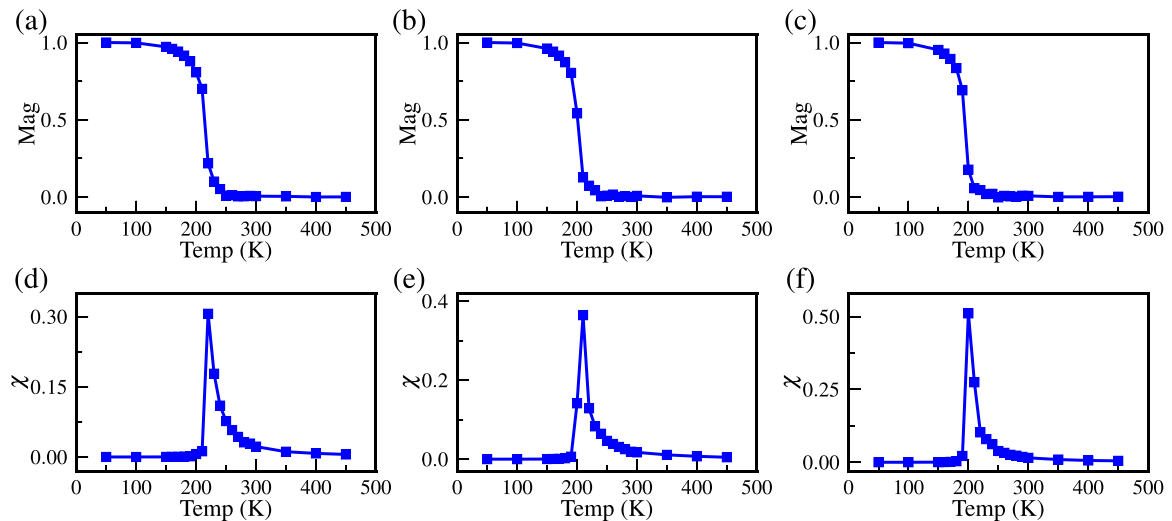


FIG. 4. The change in magnetic moment and magnetic susceptibility as a functional of temperature. The (a)–(c) correspond to variance of magnetic moment of YI₂, YBr₂, and YCl₂, respectively, whereas (d)–(f) correspond to the change in magnetic susceptibility.

As shown in Figs. 5(d)–5(f), we can see that the estimated Curie temperature of YX₂ converges with the neighbors at the eighth NN. When the 14th NN are considered, the estimated Curie temperatures of YI₂, YBr₂, and YCl₂ are 198, 118, and 95 K, respectively. Compared to the results obtained by only considering the nearest-neighbor interaction, the differences are 13.74%, 5.96%, and 3.19%. This indicates the NN mag-

netic exchange interaction is crucial to magnetic properties of YI₂, which also suggested the above assumption is reasonable.

These values are much larger than that of most of available 2D ferromagnetic materials. For example, the T_c of the recently experimental discovered 2D ferromagnetic materials CrI₃ [47,48] and Cr₂Ge₂Te₆ [49] is only 45 and 30 K. Therefore, the predicted high magnetic transition temperature of SL

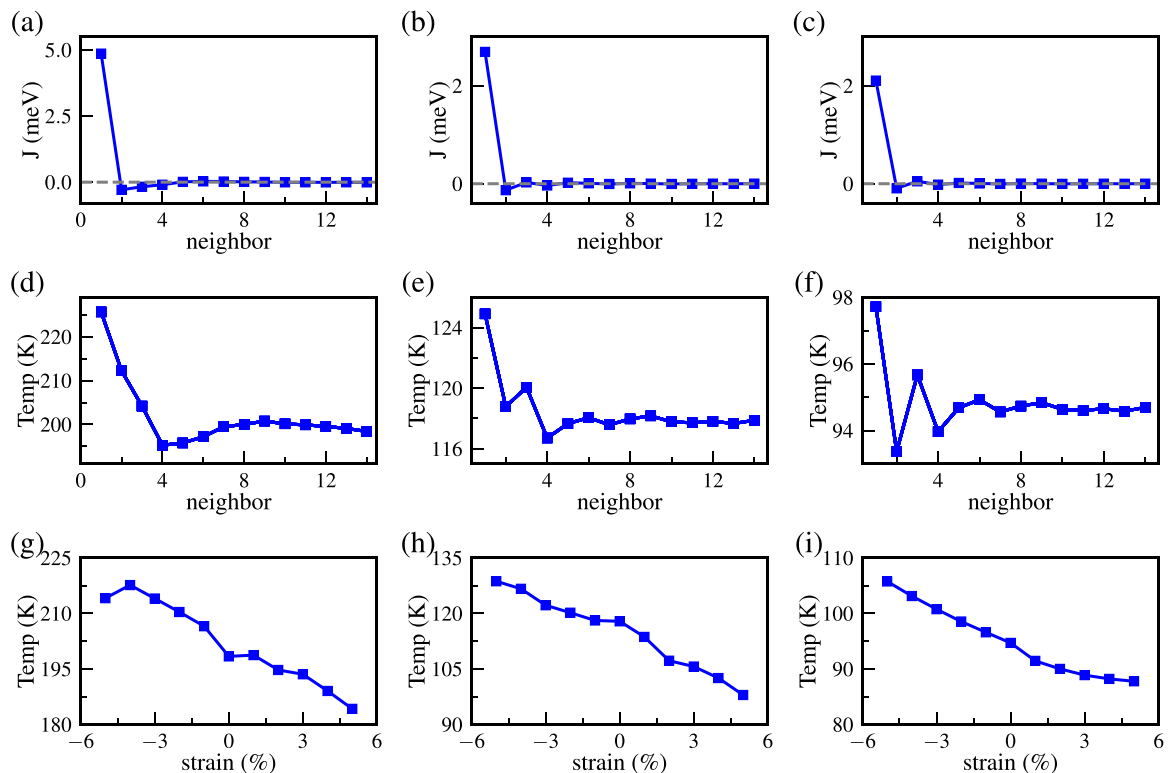


FIG. 5. The magnetic exchange coupling constants and Curie temperatures of YX₂ (X=I, Br, and Cl) under equilibrium and strain conditions. (a)–(c) represent the magnetic exchange coupling constants of YI₂, YBr₂, and YCl₂ as a function of the number of neighbors, respectively. (d)–(f) represent the estimated Curie temperatures of YI₂, YBr₂, and YCl₂ as a function of the number of neighbors considered. (g)–(i) represent the Curie temperature under different strain conditions of YI₂, YBr₂, and YCl₂ with the 14th NN exchange interaction, respectively.

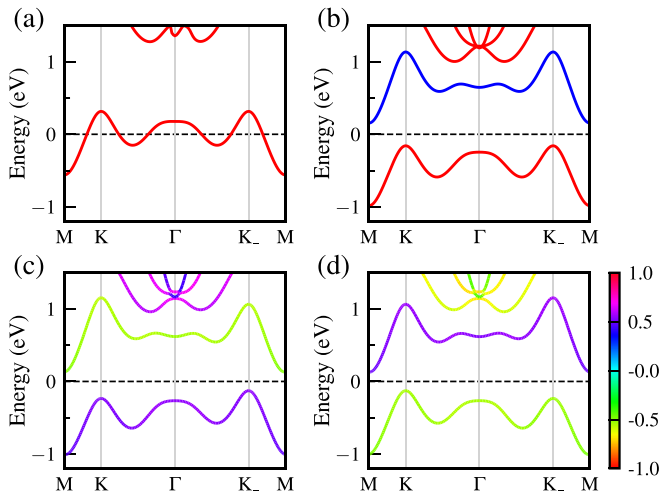


FIG. 6. The band structure of SL YI_2 . (a) Without spin polarization and SOC. (b) With spin polarization but without SOC. Red and blue lines represent the spin-up and spin-down bands. (c) with spin polarization and SOC. (d) is the same as (c) but with the opposite magnetization orientation. The Fermi level is set to 0 eV. The color bar represents the spin contribution of the energy band, in which -1 (corresponding to the lower limit) and 1 (upper limit) represent two opposite spin directions, respectively.

YX_2 is quite benefit to the practical application in valleytronics and spintronics.

C. Electronic structure and valley splitting

Now, we turn our attention to the electronic structure. Since the band structures of YX_2 are very similar, we discuss YI_2 as an illustrative example. As shown in Fig. 6(a), when neither spin polarization nor SOC is considered, a typical metallic state with a spin degenerate is found in YI_2 . Energies at K/K_+ valleys are degenerate. As shown in Fig. 6(b), when spin polarization is considered in the calculations, a sizable energy gap is formed and a clear exchange splitting can be found. The K and K_+ valleys still remain degenerate and have the same spin component. The spin splitting Δ_{spin} of YI_2 , which is defined as the energy difference between two spin directions in K/K_+ valleys is 1.30 eV. We can also find that the topmost valence band and the lowest conduction band are contributed by the spin-up and spin-down bands, respectively. SL YI_2 is, thus, a bipolar ferromagnetic semiconductor. Moreover, the valence-band maximum (VBM) is located at K or K_+ , whereas the conduction-band minimum (CBM) is located at M .

With spin polarization and SOC, the indirect semiconducting properties of SL YX_2 can still be found. The energy gap is about 0.255 eV. We also confirm the electronic structure of SL YI_2 by using more accurate hybrid functional HSE06. The band structure is similar but the gap increases to 0.711 eV. The predicted indirect band gaps of SL YX_2 ($x = \text{Br}$ and Cl) are 0.530 and 0.626 eV, respectively. Interestingly, the valley degeneracy between the K and K_+ points is lifted as shown in Fig. 6(c). A valley splitting occurred spontaneously in SL YX_2 without any external tuning. Valley polarization Δ_{val} defined as the energy difference between K and K_+ valleys of YI_2 , YBr_2 , and YCl_2 were predicted to be 108.98, 57.75,

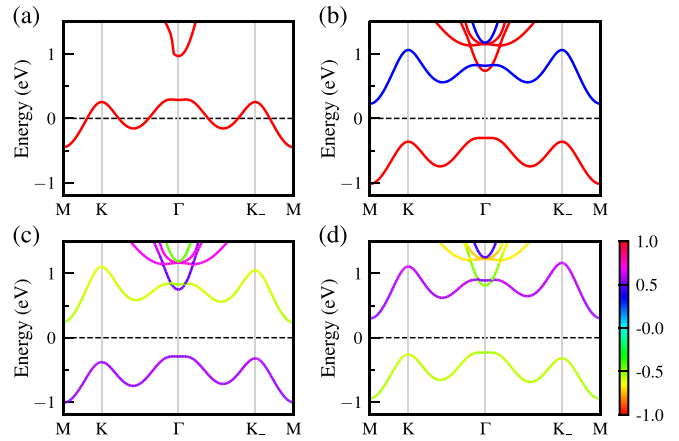


FIG. 7. The band structure of SL YBr_2 . (a) Without spin polarization and SOC. (b) With spin polarization but without SOC. Red and blue lines represent the spin-up and spin-down bands. (c) Both with spin polarization and SOC. (d) is the same as (c) but with the opposite magnetization orientation. The Fermi level is set to 0 eV.

and 22.35 meV, respectively. The valley polarization of YI_2 calculated by the HSE06 functional is as large as 122 meV. This value is much larger than those of available ferrovalley materials, such as VSe_2 (78.2 meV) [17], LaBr_2 (33 meV) [18], VSi_2N_4 (71 meV) [19], and Cr_2Se_3 (18.7 meV) [21], comparable with the values of Janus FeClF (109 meV) [50], GdI_2 (149 meV) [20], and NdSe_2 (219 meV) [22]. It should be pointed out that the prominent valley in a qualified ferrovalley material should be located at the VBM/CBM. As shown in Figs. 7 and 8, the energies of Γ of YBr_2 and YCl_2 are higher than that of K/K_+ . This indicates that the prominent K/K_+ valley is hidden, and YBr_2 and YCl_2 may be not suitable for practical valleytronics directly. When reversing magnetization orientation, the polarization states of the K valley and K_+ valley also reverse. The energy of the K valley is higher than that of the K_+ valley, and the value of valley splitting remains unchanged as shown in Fig. 6(d). Moreover,

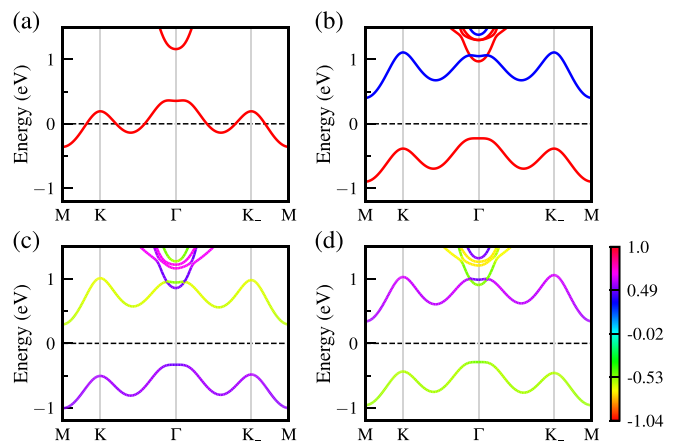


FIG. 8. The band structure of SL YCl_2 . (a) Without spin polarization and SOC. (b) With spin polarization but without SOC. Red and blue lines represent the spin-up and spin-down bands. (c) Both with spin-polarization and SOC. (d) is the same as (c) but with the opposite magnetization orientation. The Fermi level is set to 0 eV.

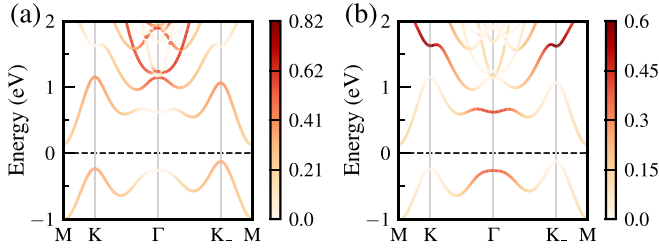


FIG. 9. The 4d orbital-resolved band structure of SL YI₂. (a) and (b) represent $d_{xy}(d_{x^2-y^2})$, and d_{z^2} , respectively. The color bar represents the weight of the orbital contributions in which the value of 1 means that the band is contributed by the band fully whereas the value of 0 means the band does not contain this orbital component at all.

we can find that the valence and conduction bands are only contributed by one spin, which is also beneficial to detection and manipulation of valley. As illustrated in Fig. 9, Figs. 10 and 11, both valleys at K and K_- are primarily contributed by d_{xy} and $d_{x^2-y^2}$ orbitals, whereas the electronic states at Γ points are mainly contributed by d_{z^2} orbitals.

The large spontaneous valley polarization in YX_2 can be sourced from the large magnetic exchange interaction and strong SOC effect. Without spin polarization and SOC, the single electron will occupy the twofold spin degenerate d_{z^2} , which forms a metallic state. With spin polarization but excluding SOC, a huge spin splitting up to 1.30 eV induced by the magnetic exchange interaction occurs. However, the energetic degeneracy between K and K_- is preserved since the $E_{\uparrow}(K) = E_{\uparrow}(K_-)$, $E_{\downarrow}(K) = E_{\downarrow}(K_-)$ in the absence of SOC. When including SOC but excluding spin polarization, SOC will induce an inequivalent valley at K and K_- in the present spatial-inversion-symmetry- broken system. But two valleys are energetically degenerate with opposite spins due to the time-reversal symmetry, i.e., $E_{\uparrow}(K) = E_{\downarrow}(K_-)$, $E_{\downarrow}(K) = E_{\uparrow}(K_-)$. With spin polarization and SOC, the time-inversion symmetry of SL YI₂ is broken, and the energy of the K and K_- valleys is no longer degenerate. The valley polarization occurs spontaneously without any external tuning. In the case of YI₂, the spin splitting caused by magnetic exchange interaction is much larger than that caused by SOC, which leads to the clean spin contribution in both the valence band and the conduction band. Moreover, according to the analysis of the orbital-resolved band, the remarkable spontaneous valley polarization in YI₂ can be understood by the relatively strong SOC effect within Y- d_{xy} and $d_{x^2-y^2}$ orbitals combined with the magnetic exchange interaction of Y- d electrons.

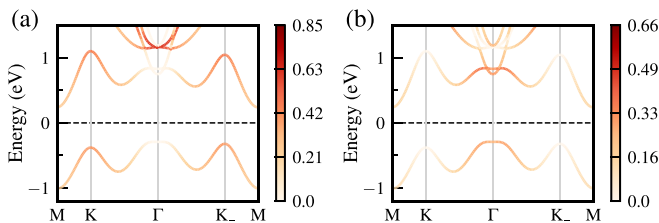


FIG. 10. The 4d orbital-resolved band structure of SL YBr₂. (a) and (b) represent $d_{xy}(d_{x^2-y^2})$ and d_{z^2} , respectively.

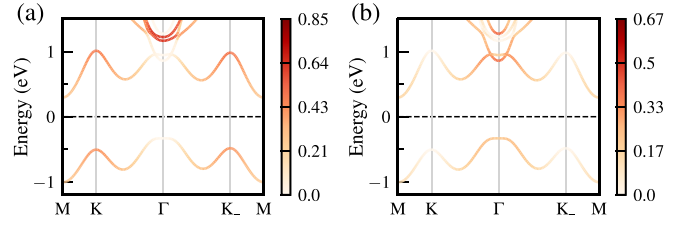


FIG. 11. The 4d orbital-resolved band structure of SL YCl₂. (a) and (b) represent $d_{xy}(d_{x^2-y^2})$ and d_{z^2} , respectively.

Moreover, we also find that the valley polarization depends on the magnetization directions. As shown in Fig. 12, the variation of valley polarization with the angle following a sine function. A large valley polarization can be realized easily by a very tiny energy cost at order of one-tenth meV.

D. Berry curvature and valley anomalous Hall effect

To reveal the valley contrasting physics in 2H-YI₂, we calculated the Berry curvature, which is defined as [51]

$$\Omega(k) = - \sum_n \sum_{n' \neq n} f_n \frac{2 \text{Im} \langle \varphi_{nk} | v_x | \varphi_{n'k} \rangle \langle \varphi_{n'k} | v_y | \varphi_{nk} \rangle}{(E_n - E_{n'})^2}, \quad (5)$$

where f_n is the Fermi-Dirac distribution function, φ_{nk} is the periodic part of the Bloch wave function with eigenvalue E_n , $v_{x/y}$ is the velocity operator along the x/y direction. In the present paper, the Berry curvatures of SL YI₂ was evaluated using the maximally localized Wannier function method. We first compared the electronic band obtained in direct DFT calculation and Wannier fitting methods. As shown in Fig. 13(a), both results matched well with each other near the Fermi level, which indicates the accuracy of the present calculation.

Berry curvature distributions in the 2D Brillouin region and along high-symmetry points are shown in Figs. 13(b) and 13(c). We can find that the Berry curvatures of K and K_- valley possess opposite signs and the absolute values are 25.663 and 28.377 Bohr², respectively. The nondegenerate and sizable Berry curvature of K/K_- valley with opposite signs leads to interesting valley contrasting physics of SL YI₂.

Due to the large valley polarization in SL YI₂, the Fermi level can shift between the energies of the valence band at the K and K_- valleys with proper hole doping. Under an

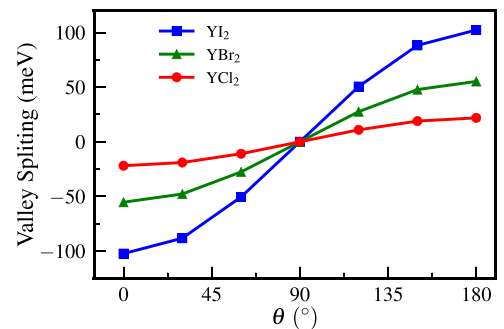


FIG. 12. The variation of valley splitting of YX_2 as a function of magnetization direction.

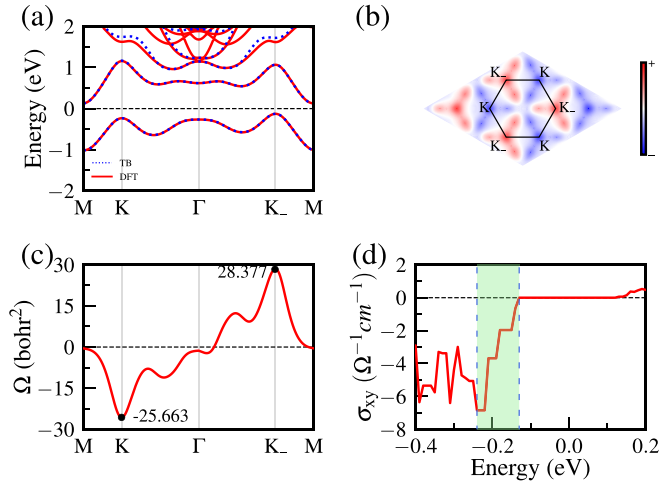


FIG. 13. The comparison of energy band of YI_2 calculated by PBE + U and Wannier fitting methods (a). The contour map for the Berry curvatures in the Brillouin zone of the SL YI_2 , and the corresponding Berry curvature along high-symmetry lines is shown in (b) and (c). Anomalous Hall conductivity as a function of energy is present in (d).

in-plane electric field, the holes at the K_- valley will acquire an anomalous velocity proportional to the Berry curvature [52], i.e., $v_{\perp} \sim E\Omega(k)$. The spin-down holes at the K_- valley will flow to the right edge of the sample. The accumulated holes on the boundary generate a charge Hall current that can be detected by a positive voltage. Otherwise, when reversing the magnetization orientation in the presence of an in-plane electric field, the spin-up holes at the K valley will flow to and be accumulated at the left edge of the sample. And transverse voltage with opposite sign (negative voltage) can be measured. The anomalous valley Hall effect, thus, can be realized in SL YI_2 . Accordingly, the valley pseudospin can be detected and manipulated selectively by electric measurement, which will provide a basis for the application of the valleytronics, such as data storage. By integrating berry curvature over the Brillouin zone,

$$\sigma_{xy} = \frac{e^2}{h} \int_{BZ} \frac{d^2k}{(2\pi)^2} f(k)\Omega(k), \quad (6)$$

one can obtain the anomalous valley Hall conductivity. As shown in Fig. 13(d), a fully spin- and valley-polarized Hall conductivity is generated in SL YI_2 .

E. Strain

Furthermore, we also investigate the ferromagnetism and valley polarization of YX_2 under a biaxial strain. Figure 2(b) gives the variation of total energy of YX_2 in FM, AFM, and NM states with different strains. Under a strain from -5% to 5% , FM is always the lowest-energy state whereas the energy of the NM state is highest. This indicates that the ground state of YX_2 is FM, which is robust to the strain.

As shown in Fig. 14(a), under the strain of -5% – 5% , the valley polarization of SL YI_2 increases gradually from 91.56 to 113.22 meV. While the result of YBr_2 (YCl_2) can also be increased from 44.23(8.35) to 65.282(32.9) meV. Neverthe-

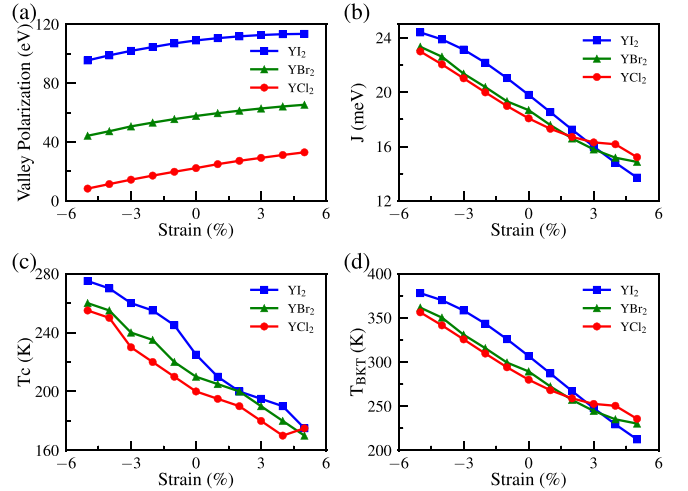


FIG. 14. (a) The valley polarization, (b) magnetic exchange constants, and (c) Curie temperature of YI_2 as a function of strains.

less, as shown in Fig. 15 we can also find that the Γ point gradually moves upwards VBM with strain, and the VBM will change from K/K_- to Γ . For YI_2 , the energy of Γ is still lower than K and K_- valleys in the range of -5% – 3% but become larger with the tensile strain above 3% . For YBr_2 and YCl_2 , the corresponding threshold value of VBM transition is -1% and -3% . When compress strain are larger than the value, the K/K_- valleys turn into the VBM, and the valley physics of YBr_2 and YCl_2 will be accessible.

We also evaluate the effect of strain on magnetic transition temperatures. As shown in Figs. 14(b) and 14(c), the magnetic exchange interaction and magnetic transition temperatures gradually decrease with strain. The Curie temperatures under different strains are also estimated using Eq. (4) with magnetic exchange interaction up to the 14th NN calculated by MFT [as shown in Figs. 5(g)–5(i)]. Similar results are found, which indicate our calculations are reliable.

As shown in Figs. 14(c) and 14(d), Curie temperature of 280 K (T_{BKT} of 370 K) can be achieved in YI_2 with a compression strain of -5% . Even with tensile strain of 5% , Curie temperature of the YI_2 is still larger than 160 K (T_{BKT} of 212 K). Considered the enhanced magnetic transition temperature and induced transition of VBM between Γ and K/K_- , compression strain is, thus, suggested as a efficient strategy to tune the performance of valleytronics of YX_2 .

IV. CONCLUSION

To summarize, we have determined that single-layer 2H- YX_2 ($X = I, Br, \text{ and } Cl$) are a series of stable two-dimensional ferrovalley semiconductors with a pair of energy valleys at K and K_- . Valley splitting occurs in YX_2 spontaneously due to intrinsic magnetic exchange interactions and strong SOC. A large valley splitting of 108.98 meV was predicted in YI_2 . The anomalous valley Hall effects are then proposed in YX_2 under in-plane electric field. In addition, compression strain is found to increase magnetic transition temperature and improve the performance of YX_2 in valleytronics. Our paper provides a series of promising candidates for the realization of spontaneous

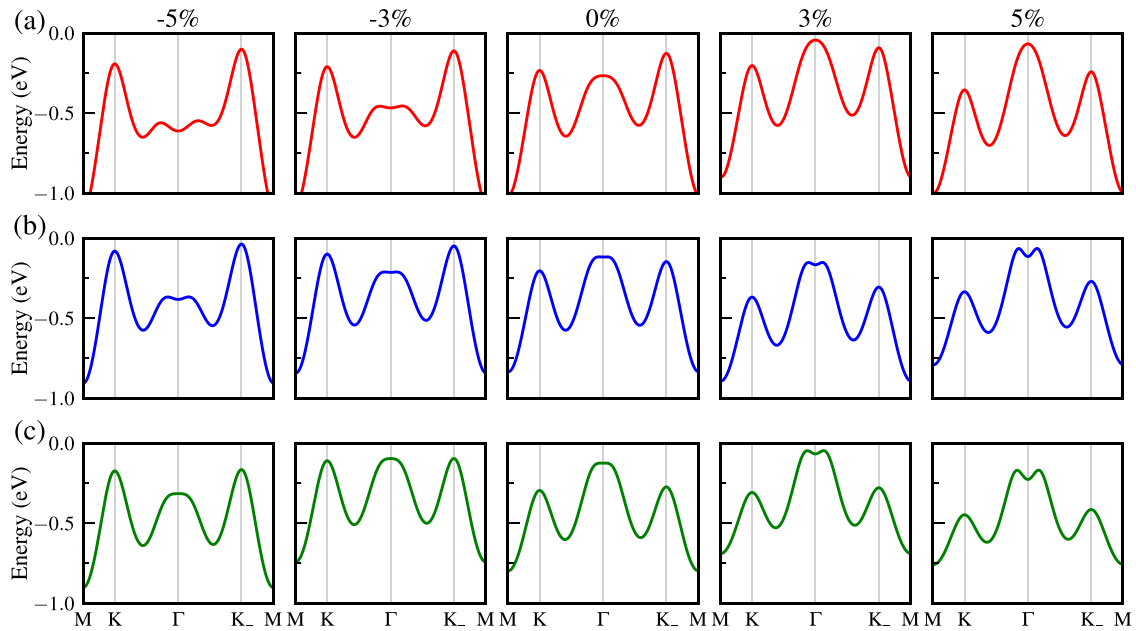


FIG. 15. The variance of band structure of YX_2 as a functional of biaxial strains. (a)–(c) corresponds the results of YI_2 , YBr_2 , and YCl_2 .

valley polarization and controllable valley electronic devices, which is also expected to be verified experimentally in the near future.

ACKNOWLEDGMENTS

This work was supported by National Natural Science Foundation of China (Grant No. 11874092), the Fok Ying-Tong Education Foundation, China (Grant No. 161005), the

Science Fund for Distinguished Young Scholars of Hunan Province (Grant No. 2021JJ10039), the Planned Science and Technology Project of Hunan Province (Grant No. 2017RS3034), Hunan Provincial Natural Science Foundation of China (Grant No. 2019JJ50636), Scientific Research Fund of Hunan Provincial Education Department (Grant No. 18C0227), and the Open Research Fund of Key Laboratory of Low-Dimensional Quantum Structures and Quantum Control of Ministry of Education (Grant No. QSQC1902).

- [1] X. Xu, W. Yao, D. Xiao, and T. F. Heinz, Spin and pseudospins in layered transition metal dichalcogenides, *Nat. Phys.* **10**, 343 (2014).
- [2] J. R. Schaibley, H. Yu, G. Clark, P. Rivera, J. S. Ross, K. L. Seyler, W. Yao, and X. Xu, Valleytronics in 2d materials, *Nat. Rev. Mater.* **1**, 16055 (2016).
- [3] G.-B. Liu, D. Xiao, Y. Yao, X. Xu, and W. Yao, Electronic structures and theoretical modelling of two-dimensional group-vib transition metal dichalcogenides, *Chem. Soc. Rev.* **44**, 2643 (2015).
- [4] D. Xiao, W. Yao, and Q. Niu, Valley-Contrasting Physics in Graphene: Magnetic Moment and Topological Transport, *Phys. Rev. Lett.* **99**, 236809 (2007).
- [5] D. Xiao, G.-B. Liu, W. Feng, X. Xu, and W. Yao, Coupled Spin and Valley Physics in Monolayers of mos_2 and other Group-vi Dichalcogenides, *Phys. Rev. Lett.* **108**, 196802 (2012).
- [6] W. Yao, D. Xiao, and Q. Niu, Valley-dependent optoelectronics from inversion symmetry breaking, *Phys. Rev. B* **77**, 235406 (2008).
- [7] H.-Z. Lu, W. Yao, D. Xiao, and S.-Q. Shen, Intervalley Scattering and Localization Behaviors of Spin-Valley Coupled Dirac Fermions, *Phys. Rev. Lett.* **110**, 016806 (2013).
- [8] H. Zeng, J. Dai, W. Yao, D. Xiao, and X. Cui, Valley polarization in Mos_2 monolayers by optical pumping, *Nat. Nanotechnol.* **7**, 490 (2012).
- [9] T. Cao, G. Wang, W. Han, H. Ye, C. Zhu, J. Shi, Q. Niu, P. Tan, E. Wang, B. Liu, and J. Feng, Valley-selective circular dichroism of monolayer molybdenum disulphide, *Nat. Commun.* **3**, 887 (2012).
- [10] Y. Li, J. Ludwig, T. Low, A. Chernikov, X. Cui, G. Arefe, Y. D. Kim, A. M. van der Zande, A. Rigosi, H. M. Hill, S. H. Kim, J. Hone, Z. Li, D. Smirnov, and T. F. Heinz, Valley Splitting and Polarization by the Zeeman Effect in Monolayer $mose_2$, *Phys. Rev. Lett.* **113**, 266804 (2014).
- [11] D. MacNeill, C. Heikes, K. F. Mak, Z. Anderson, A. Kormányos, V. Zólyomi, J. Park, and D. C. Ralph, Breaking of Valley Degeneracy by Magnetic Field in Monolayer $mose_2$, *Phys. Rev. Lett.* **114**, 037401 (2015).
- [12] G. Aivazian, Z. Gong, A. M. Jones, R.-L. Chu, J. Yan, D. G. Mandrus, C. Zhang, D. Cobden, W. Yao, and X. Xu, Magnetic control of valley pseudospin in monolayer Wse_2 , *Nat. Phys.* **11**, 148 (2015).
- [13] Y. C. Cheng, Q. Y. Zhang, and U. Schwingenschlögl, Valley polarization in magnetically doped single-layer transition-metal dichalcogenides, *Phys. Rev. B* **89**, 155429 (2014).

- [14] J. Qi, X. Li, Q. Niu, and J. Feng, Giant and tunable valley degeneracy splitting in mote_2 , *Phys. Rev. B* **92**, 121403(R) (2015).
- [15] T. Norden, C. Zhao, P. Zhang, R. Sabirianov, A. Petrou, and H. Zeng, Giant valley splitting in monolayer ws_2 by magnetic proximity effect, *Nat. Commun.* **10**, 4163 (2019).
- [16] W.-Y. Tong, S.-J. Gong, X. Wan, and C.-G. Duan, Concepts of ferrovalley material and anomalous valley hall effect, *Nat. Commun.* **7**, 13612 (2016).
- [17] J. Liu, W.-J. Hou, C. Cheng, H.-X. Fu, J.-T. Sun, and S. Meng, Intrinsic valley polarization of magnetic VSe_2 monolayers, *J. Phys.: Condens. Matter* **29**, 255501 (2017).
- [18] P. Zhao, Y. Ma, C. Lei, H. Wang, B. Huang, and Y. Dai, Single-layer LaBr_2 : Two-dimensional valleytronic semiconductor with spontaneous spin and valley polarizations, *Appl. Phys. Lett.* **115**, 261605 (2019).
- [19] Q. Cui, Y. Zhu, J. Liang, P. Cui, and H. Yang, Spin-valley coupling in a two-dimensional Vsi_2n_4 monolayer, *Phys. Rev. B* **103**, 085421 (2021).
- [20] H.-X. Cheng, J. Zhou, W. Ji, Y.-N. Zhang, and Y.-P. Feng, Two-dimensional intrinsic ferrovalley Gdi_2 with large valley polarization, *Phys. Rev. B* **103**, 125121 (2021).
- [21] Z. He, R. Peng, X. Feng, X. Xu, Y. Dai, B. Huang, and Y. Ma, Two-dimensional valleytronic semiconductor with spontaneous spin and valley polarization in single-layer cr_2se_3 , *Phys. Rev. B* **104**, 075105 (2021).
- [22] Y. Zang, Y. Ma, R. Peng, H. Wang, B. Huang, and Y. Dai, Large valley-polarized state in single-layer NbX_2 ($x = \text{s, se}$): Theoretical prediction, *Nano Res.* **14**, 834 (2021).
- [23] H. Huan, Y. Xue, B. Zhao, G. Gao, H. Bao, and Z. Yang, Strain-induced half-valley metals and topological phase transitions in $m\text{br}_2$ monolayers ($m = \text{Ru, Os}$), *Phys. Rev. B* **104**, 165427 (2021).
- [24] S. Hastrup, M. Strange, M. Pandey, T. Deilmann, P. S. Schmidt, N. F. Hinsche, M. N. Gjerding, D. Torelli, P. M. Larsen, A. C. Riis-Jensen, J. Gath, K. W. Jacobsen, J. J. Mortensen, T. Olsen, and K. S. Thygesen, The computational 2d materials database: high-throughput modeling and discovery of atomically thin crystals, *2D Mater.* **5**, 042002 (2018).
- [25] M. N. Gjerding, A. Taghizadeh, A. Rasmussen, S. Ali, F. Bertoldo, T. Deilmann, N. R. Knøsgaard, M. Kruse, A. H. Larsen, S. Manti, T. G. Pedersen, U. Petralanda, T. Skovhus, M. K. Svendsen, J. J. Mortensen, T. Olsen, and K. S. Thygesen, Recent progress of the computational 2d materials database (c2db), *2D Mater.* **8**, 044002 (2021).
- [26] G. Kresse and J. Furthmüller, Efficiency of ab-initio total energy calculations for metals and semiconductors using a plane-wave basis set, *Comput. Mater. Sci.* **6**, 15 (1996).
- [27] G. Kresse and J. Furthmüller, Efficient iterative schemes for ab initio total-energy calculations using a plane-wave basis set, *Phys. Rev. B* **54**, 11169 (1996).
- [28] P. E. Blöchl, Projector augmented-wave method, *Phys. Rev. B* **50**, 17953 (1994).
- [29] G. Kresse and D. Joubert, From ultrasoft pseudopotentials to the projector augmented-wave method, *Phys. Rev. B* **59**, 1758 (1999).
- [30] J. P. Perdew, K. Burke, and M. Ernzerhof, Generalized Gradient Approximation Made Simple, *Phys. Rev. Lett.* **77**, 3865 (1996).
- [31] S. L. Dudarev, G. A. Botton, S. Y. Savrasov, C. J. Humphreys, and A. P. Sutton, Electron-energy-loss spectra and the structural stability of nickel oxide: an lsda+u study, *Phys. Rev. B* **57**, 1505 (1998).
- [32] J. Heyd, G. E. Scuseria, and M. Ernzerhof, Hybrid functionals based on a screened coulomb potential, *J. Chem. Phys.* **118**, 8207 (2003).
- [33] A. V. Krukau, O. A. Vydrov, A. F. Izmaylov, and G. E. Scuseria, Influence of the exchange screening parameter on the performance of screened hybrid functionals, *J. Chem. Phys.* **125**, 224106 (2006).
- [34] H. J. Monkhorst and J. D. Pack, Special points for brillouin-zone integrations, *Phys. Rev. B* **13**, 5188 (1976).
- [35] A. Togo, F. Oba, and I. Tanaka, First-principles calculations of the ferroelastic transition between rutile-type and CaCl_2 -type SiO_2 at high pressures, *Phys. Rev. B* **78**, 134106 (2008).
- [36] G. Pizzi, V. Vitale, R. Arita, S. Blügel, F. Freimuth, G. Géranton, M. Gibertini, D. Gresch, C. Johnson, T. Koretsune, J. Ibañez-Azpiroz, H. Lee, J.-M. Lihm, D. Marchand, A. Marrazzo, Y. Mokrousov, J. I. Mustafa, Y. Nohara, Y. Nomura, L. Paulatto *et al.*, Wannier90 as a community code: new features and applications, *J. Phys.: Condens. Matter* **32**, 165902 (2020).
- [37] A. A. Mostofi, J. R. Yates, G. Pizzi, Y.-S. Lee, I. Souza, D. Vanderbilt, and N. Marzari, An updated version of wannier90: A tool for obtaining maximally-localised wannier functions, *Comput. Phys. Commun.* **185**, 2309 (2014).
- [38] T. Oguchi, K. Terakura, and A. R. Williams, Band theory of the magnetic interaction in mno , mns , and nio , *Phys. Rev. B* **28**, 6443 (1983).
- [39] A. Liechtenstein, M. Katsnelson, V. Antropov, and V. Gubanov, Local spin density functional approach to the theory of exchange interactions in ferromagnetic metals and alloys, *J. Magn. Magn. Mater.* **67**, 65 (1987).
- [40] M. J. Han, T. Ozaki, and J. Yu, Electronic structure, magnetic interactions, and the role of ligands in mn_n ($n = 4, 12$) single-molecule magnets, *Phys. Rev. B* **70**, 184421 (2004).
- [41] T. Ozaki, Variationally optimized atomic orbitals for large-scale electronic structures, *Phys. Rev. B* **67**, 155108 (2003).
- [42] H. Yoon, T. J. Kim, J.-H. Sim, S. W. Jang, T. Ozaki, and M. J. Han, Reliability and applicability of magnetic-force linear response theory: Numerical parameters, predictability, and orbital resolution, *Phys. Rev. B* **97**, 125132 (2018).
- [43] H. Yoon, T. J. Kim, J.-H. Sim, and M. J. Han, Jx: An open-source software for calculating magnetic interactions based on magnetic force theory, *Comput. Phys. Commun.* **247**, 106927 (2020).
- [44] J. Wang, S. Yip, S. R. Phillpot, and D. Wolf, Crystal Instabilities at Finite Strain, *Phys. Rev. Lett.* **71**, 4182 (1993).
- [45] J. B. Goodenough, *Magnetism and the Chemical Bond* (Interscience-Wiley, New York, 1963).
- [46] A. Terasawa, M. Matsumoto, T. Ozaki, and Y. Gohda, Efficient algorithm based on liechtenstein method for computing exchange coupling constants using localized basis set, *J. Phys. Soc. Jpn.* **88**, 114706 (2019).
- [47] W.-B. Zhang, Q. Qu, P. Zhu, and C.-H. Lam, Robust intrinsic ferromagnetism and half semiconductivity in stable two-dimensional single-layer chromium trihalides, *J. Mater. Chem. C* **3**, 12457 (2015).
- [48] B. Huang, G. Clark, E. Navarro-Moratalla, D. R. Klein, R. Cheng, K. L. Seyler, D. Zhong, E. Schmidgall, M. A. McGuire,

- D. H. Cobden, W. Yao, D. Xiao, P. Jarillo-Herrero, and X. Xu, Layer-dependent ferromagnetism in a van der waals crystal down to the monolayer limit, *Nature (London)* **546**, 270 (2017).
- [49] C. Gong, L. Li, Z. Li, H. Ji, A. Stern, Y. Xia, T. Cao, W. Bao, C. Wang, Y. Wang, Z. Q. Qiu, R. J. Cava, S. G. Louie, J. Xia, and X. Zhang, Discovery of intrinsic ferromagnetism in two-dimensional van der waals crystals, *Nature (London)* **546**, 265 (2017).
- [50] S.-D. Guo, J.-X. Zhu, M.-Y. Yin, and B.-G. Liu, Substantial electronic correlation effects on the electronic properties in a janus fecl₂ monolayer, *Phys. Rev. B* **105**, 104416 (2022).
- [51] D. J. Thouless, M. Kohmoto, M. P. Nightingale, and M. den Nijs, Quantized Hall Conductance in a Two-Dimensional Periodic Potential, *Phys. Rev. Lett.* **49**, 405 (1982).
- [52] D. Xiao, M.-C. Chang, and Q. Niu, Berry phase effects on electronic properties, *Rev. Mod. Phys.* **82**, 1959 (2010).